

Synthesis and characterization of Barium ferrite nano-particles for X-ray/gamma radiation shielding and display applications

B. Chinnappa Reddy ^{a,b}, Y.S. Vidya ^{c,*}, H.C. Manjunatha ^{d,*}, K.N. Sridhar ^e, U. Mahaboob Pasha ^a, L. Seenappa ^d, B. Sadashivamurthy ^e, N. Dhananjaya ^f, B.M. Sankarshan ^g, S. Krishnaveni ^h, K.V. Sathish ^d, P.S. Damodara Gupta ^d

^a Department of Physics, Presidency University, Bengaluru 560064, Karnataka, India

^b Department of Physics, Government First Grade College, Srinivasapur 563135, Karnataka, India

^c Department of Physics, Lal Bahadur Shastri Government First Grade College, RT Nagar, Bangalore 560032, Karnataka, India

^d Department of Physics, Government College for Women, Kolar 563101, Karnataka, India

^e Department of Physics, Government First Grade College, Kolar 563101, Karnataka, India

^f Department of Physics, BMS Institute of Technology and Management, Bangalore 560064, Karnataka, India

^g Department of Physics, The National Institute of Engineering, Mysuru 570008, Karnataka, India

^h Department of Physics, University of Mysore, Mysuru 570006, Karnataka, India



ARTICLE INFO

Keywords:

BaFe₂O₄

Solution combustion method

Shielding properties

Photoluminescence

ABSTRACT

In the present communication, BaFe₂O₄ (BFO) nanoparticles were synthesized by solution combustion method using urea as a fuel and calcined at 500 °C for 3 h. To know the phase purity, functional group, surface morphology, structural analysis and energy band gap, the synthesized sample was characterized by using the techniques such as powder X-ray diffraction (PXRD), Scanning electron microscopy (SEM), Fourier transmission infrared spectroscopy (FTIR) and UV-Visible spectrophotometer. The Bragg's reflection of PXRD confirms the formation of orthorhombic spinel crystal structure with space group *Cmc21(36)*. In addition to orthorhombic phase, additional PXRD peaks corresponding to monoclinic phase of BFO were also observed. Wood and Tauc's relation was used to calculate direct energy band gap and was found to be 5.2 eV. Photoluminescence studies ($\lambda_{ex} = 350$ nm), CIE and CCT values revealed that the present BFO nanomaterial could meet the needs of illumination devices. In addition, X-ray/gamma ray shielding properties of BFO nanoparticles in the energy range 0.081–1.332 MeV have been measured using NaI (Tl) detector and PC based multi channel analyser (MCA). The measured shielding parameters are compared with the standard theoretical values. It is found that above 356 keV energy of gamma ray, the measured shielding parameters agrees well with the theory, whereas, slight deviation is observed below 356 keV. This deviation may be mainly attributed to the particle size of the target medium. Furthermore, an accurate theory is necessary to explain the interaction of X-ray/gamma with the nano size atoms. The present work opens new window to use this facile, economical, efficient, low temperature method to synthesize nanomaterials for X-ray/gamma ray shielding purpose as well as the display device applications.

1. Introduction

Now-a-days the application of nanomaterials (NMs) are found in every field of science and technology. The researchers are fascinated and working for the advancement of the nanoscience in terms of size, capability and cost effectiveness. Their high surface to volume ratio over the bulk materials offers outstanding physicochemical, electrical, optical, magnetic and quantum properties (Barros and Casey, 2020; Gatoo et al., 2014; Choi, 2017; Jonnalagadda et al., 2021; Kannan et al., 2021; Hodala et al., 2021; Shanmugan et al., 2020; Reddy et al.,

2020; Karthik et al., 2019; Srinivas et al., 2019). Their applications range from medical to modern industries. They are used in the field of sensors, solar cells, display technology, information technologies, agriculture, industry, medical for diagnosis and drug delivery, electro magnetic shielding as a shielding material, waste water treatment as a catalyst, energy storage devices etc (Chen et al., 2020; Kaphle et al., 2018; Pellico et al., 2021; Suárez-Iglesias et al., 2017; Kumar, 2019). In addition to all these applications, these NMs plays a significant role as

* Corresponding authors.

E-mail addresses: vidays.phy@gmail.com (Y.S. Vidya), manjunathhc@rediffmail.com (H.C. Manjunatha).

multi functional radiation-shielding materials in space (Thibeault et al., 2015).

Among different types of NMs, ferrites which are large class of oxides with remarkable magnetic properties finds diverse applications, particularly in magnetic recording media components, permanent magnets, photocatalysts, high frequency applications, coherent spin FET, ceramic pigments, microwave absorbers and magnetic sensors (Dimri et al., 2019; Chang et al., 2012; Slusarek and Zakrzewski, 2012; Bhavikatti et al., 2010). These ferrites shows variety of interesting properties such as high electrical resistivity, low electrical losses and a very good chemical stability (Valenzuela, 2012). In general, the spinel ferrite based materials has face centred cubic structure in which oxygen atoms are cubic close packed, the magnetic ions are distributed among two dissimilar lattice sites, tetrahedral (A) and octahedral (B) sites. The ferrite has 32 octahedral and 64 tetrahedral sites. Each lattice of unit cell contains 16 octahedral sites occupied by trivalent iron atoms and 8 tetrahedral sites occupied by metal divalent atoms (Kumar et al., 2018). Among the ferrites, BaFe_2O_4 (Barium ferrite) (BFO) shows interesting soft magnetic properties with high electrical resistivity.

Recently many researchers synthesized different ferrite systems; $\text{Co}_{0.6}\text{Zn}_{0.4}\text{Mn}_{2x}\text{Fe}_{2x}\text{O}_4$ (Hamada, 2004), $\text{Li}_{0.5}\text{Fe}_{2.5}\text{O}_4$ (Mane et al., 2011), $\text{Mn}_{0.5}\text{Zn}_{0.5}\text{Fe}_2\text{O}_4$ (Angadi et al., 2017), $\text{Ni}_{1x}\text{Zn}_x\text{Fe}_2\text{O}_4$ spinel ferrite (Karim et al., 2010), $\text{Ni}_{1x}\text{Zn}_x\text{Fe}_{2x}\text{Cr}_x\text{O}_4$, (Ni-Zn-Cr) NPs (Mande et al., 2019) and studied the effect of gamma irradiation on the structural, electrical and magnetic properties. In the past decade, a number of ferrites like Ba, Mn, Ni, Co, Zn, $\gamma\text{-Fe}_2\text{O}_3$ and their composites (Gairola et al., 2010; Ohlan et al., 2008; Singh et al., 2008) were used for microwave shielding materials because it offers good magnetic properties (Li et al., 2013; Qiu et al., 2005). Recently researchers have evaluated shielding parameters for heavy metal fluoride based tellurite-rich glasses for gamma ray shielding applications (Sayyed et al., 2017). BFO has been experimented for shielding of electromagnetic radiation (Gairola et al., 2016). Theoretically the effective atomic numbers (Z_{eff}) and effective electron density (N_e) of BFO and Barium hexaferrite ($\text{BaFe}_{12}\text{O}_{19}$) were determined (Raut et al., 2017). Yet gamma ray shielding properties on synthesized BFO NMs has not been reported in the literature.

It is very important to replace lead and lead compounds with other compounds which are less toxic for X-ray and gamma ray shielding. Studying the behaviour of NMs and nanocomposites when they interact with X-rays and gamma rays would throw light in this regard and helps to find out the phantom materials which could replace the lead based compounds. The quality and quantity of synthesized NPs, as well as their characterization and applications, are greatly influenced by several factors such as the synthesis process, pH, temperature, strain, time, particle size, pore size, environment and proximity (Patra and Baek, 2014). Different methods have been employed to synthesize BFO NPs such as co-precipitation (Akther Hossain et al., 2004), sol-gel (Rafique et al., 2016), reactive milling (Gabal et al., 2014), sonochemical (Goswami et al., 2013), solvothermal (Bateer et al., 2014), ultrasonic (Chen et al., 2012), thermal decomposition (Naseri et al., 2011), hydrothermal technique (Hou et al., 2010) to investigate the structural, morphological properties. These traditional methods can be used to produce large amounts of NPs with fixed sizes and shapes in a short span of time. However, these methods are complex, expensive, unreliable and outdated. To solve this issue solution combustion method was used.

Considerable efforts have been made to develop an effective nanophosphor in modern display technology and a best X-ray/gamma ray shielding material. In BFO NMs, Barium and Iron is found to be mechanically, chemically and structurally stable material and is also expected to be good absorber of X-ray/gamma ray radiation. These BFO NMs possess wide absorption, less energy band gap. Analogous to this, we expect good absorption of X-ray/gamma radiation by the BFO nanoparticles. Hence in the present work, we have synthesized BFO NMs for the purpose of X-ray/gamma radiation shielding and



Fig. 1. Flow chart for the synthesis of BFO NPs using urea as a fuel.

display applications. In the present work, we have synthesized small size (16 to 22 nm) barium ferrite nanoparticles using a low cost economical solution combustion method. The synthesized nanoparticles were studied for photoluminescence studies. In addition to this, X-ray/gamma shielding parameters are established. The established shielding parameters data on barium ferrite nanoparticles are useful in radiation protection. It is very important to replace lead and lead compounds by other compounds which are less toxic for X ray and gamma ray shielding. Studying the behaviour of nanomaterials and nanocomposites when they interact with x rays and gamma rays would through light in this regard and helps to find out the phantom materials which could replace the lead based compounds. Present work consist of two parts, in the first part, we have synthesized and characterized the BFO NPs. In the second part, we have measured the radiation shielding properties and display properties. To the best of our knowledge, low temperature solution combustion synthesis was demonstrated to be a versatile and energy efficient method for preparing BFO NMs for the first time. The obtained nanopowders were characterized using X-ray diffraction (XRD), scanning electron microscopy (SEM), Fourier transmission infrared spectroscopy (FTIR) and UV-Visible absorption spectroscopy. Due to its excellent optical, electronic and structural properties, photoluminescence studies and X-ray/gamma ray shielding properties of synthesized BFO NMs calcined at 500 °C are discussed in detail.

2. Materials and methods

2.1. Synthesis and characterization of BFO nanoparticles

Barium nitrate [$\text{Ba}(\text{NO}_3)_2 \cdot 6\text{H}_2\text{O}$], Iron(III) nitrate [$\text{Fe}(\text{NO}_3)_3 \cdot 9\text{H}_2\text{O}$] and Urea [$\text{CH}_4\text{N}_2\text{O}$] with 99.9% purity were obtained from Sdfine chemicals. All the reagents were of analytical grade and used as such without further purification. BFO NPs were synthesized by solution combustion method using Urea as fuel. Stoichiometric quantity of mixture containing Barium nitrate [$\text{Ba}(\text{NO}_3)_2 \cdot 6\text{H}_2\text{O}$], Iron(III) nitrate [$\text{Fe}(\text{NO}_3)_3 \cdot 9\text{H}_2\text{O}$] and fuel Urea [$\text{CH}_4\text{N}_2\text{O}$] were taken in a cylindrical crucible. The mixture was stirred well in order to obtain homogeneity for half an hour at 400 rpm. This crucible was placed in preheated muffle furnace maintained at a temperature of 500 ± 10 °C. The resulting solution was initially boiled, subsequently dehydrated with elimination of gases like carbon dioxide, nitrogen and water vapour followed by the formation of final product. The resultant product was calcined at 500 °C for 3 h and then it was cooled to the room temperature and collected. Fig. 1 gives the pictorial representation or the flow chart for the synthesis of BFO NPs using urea as a fuel.

The characterization of the final product followed by measurement of X-ray/gamma ray shielding properties of multi functional nickel ferrite and the theoretical evaluation was explained briefly in our previous work (Reddy et al., 2021). The schematic view of the experimental set up used for the measurement of X-ray/gamma ray shielding properties of BFO is provided in Fig. 2. The sample was directly attached to the opening of the lead shield where source is placed. The integral intensities, I_0 and I of the beam before and after passing through the

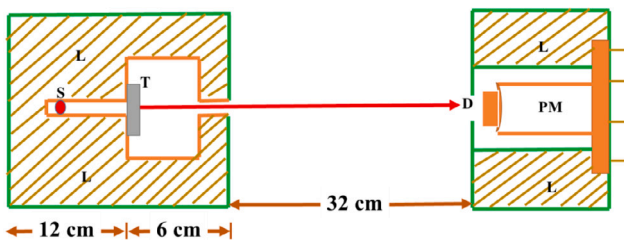


Fig. 2. Schematic diagram of the Experimental Setup (S: Source position, T: Target sample, L: Lead shielding, D: Detector, PM: Photomultiplier).

sample are measured for sufficient time. Mass attenuation coefficient of the sample is then estimated using the relation:

$$\left(\frac{\mu}{\rho}\right)_c = \left(\frac{1}{t\rho}\right) \ln\left(\frac{I_0}{I}\right) \quad (1)$$

Where t and ρ are the thickness and density of the sample respectively. When we record the spectrum without any target the spectral lines that we get is only due to the radioactive source, in the present case it is the gamma radiation. But when we keep the target due to interaction of gamma rays with that of the target material there will be an emission of secondary X-rays. We can distinguish this if record the two spectrum viz., with sample between the source and the detector and another only with the source. Theoretically, mass attenuation coefficient (MAC) (μ/ρ) are generated using WinXCom code (Manjunatha, 2015). The total linear attenuation coefficient (LAC) (μ) can be calculated by multiplying the density of the compounds with (μ/ρ) (Manjunatha et al., 2019). Half value layer (HVL), tenth value layer (TVL) and mean free path (λ) are computed from following set of equations;

$$HVL = \frac{\ln 2}{\mu} = \frac{0.693}{\mu} \quad (2)$$

$$TVL = \frac{\ln 10}{\mu} = \frac{2.303}{\mu} \quad (3)$$

$$\lambda = \frac{\int_0^\infty x \exp(-\mu x) dx}{\int_0^\infty \exp(-\mu x) dx} = \frac{1}{\mu} \quad (4)$$

Our Previous work (Manjunatha, 2015; Seenappa et al., 2017; Manjunatha, 2017; Manjunatha et al., 2017; Rudraswamy et al., 2010; Manjunatha et al., 2016; Manjunatha, 2014; Manjunatha and Rudraswamy, 2013; Suresh et al., 2008; Manjunatha and Rudraswamy, 2011, 2012) clearly explained the method and equations used in estimating the effective atomic number (Z_{eff}) and effective electron density (N_e). We have adopted the methodology given by the previous researchers for the evaluation of Specific gamma ray constant (Γ) (Ioan et al., 2018), Radiation protection efficiency (RPE) (Rammah et al., 2020), Energy absorption build up factor (EABF) (Manjunatha et al., 2019) Kerma coefficients (El-Khayatt, 2017), and Specific absorbed fraction of energy (SAF) (Suresh et al., 2007; Gerward et al., 2004; Manjunatha and Rudraswamy, 2011, 2013).

3. Results and discussion

In the present study, BFO samples have been synthesized by economical solution combustion method using urea as a fuel and calcined at 500 °C. To know the phase purity, functional group, surface morphology, structural analysis and energy band gap, the synthesized sample was characterized by using the techniques such as PXRD, SEM, EDAX, FTIR and UV-Visible spectrophotometer. To the best of our knowledge, for the first time, an attempt has been made to develop an efficient nanophosphor and a good X-ray/gamma ray material. Thus, photoluminescence and X-ray/Gamma ray shielding properties of synthesized BFO NPs are discussed in detail.

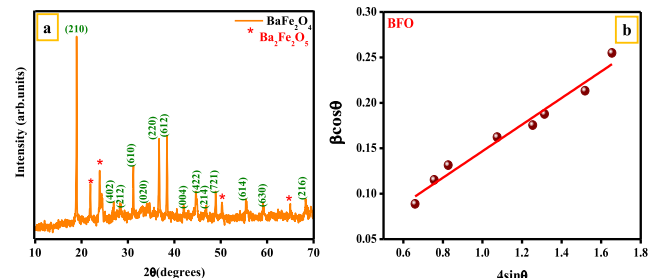


Fig. 3. (a) PXRD pattern and (b) W-h plot of BFO NPs calcined at 500 °C for 3 h.

3.1. PXRD analysis of BFO nanoparticles

PXRD is one of the most extensively used techniques for the characterization of NPs. It provides the information about the crystalline structure, phase nature, lattice parameters and crystalline grain size. Fig. 3 depicts the PXRD pattern of BFO NMs synthesized by facile solution combustion method calcined at 500 °C for 3 h. The sharp diffraction planes clearly confirms the high crystallinity of the sample. The calcined sample exhibits hkl planes (210), (402), (212), (610), (020), (220), (612), (004), (422), (214), (721), (614), (630) and (216) at 19°, 27°, 28.46°, 31.07°, 34.39°, 36.7°, 38.4°, 41.9°, 44.63°, 46.9°, 48.9°, 55.35°, 59.14° and 68.26° 2θ values. These (hkl) planes matches well with JCPDS number 00-046-0113 (Peymanfar et al., 2018) with orthorhombic spinel crystal structure having a space group Cmc21(36) with lattice parameters $a = 8.454$ Å, $b = 19.04$ Å and $c = 5.38$ Å. In addition to orthorhombic phase, additional PXRD peaks are observed at 21.8°, 23.8°, 50.14° and 64.9° 2θ values which corresponds to monoclinic phase of BFO ($\text{Ba}_2\text{Fe}_2\text{O}_5$) (Liu et al., 2018). As per Candeia et al. (2007), the PXRD pattern of BFO synthesized by Pechini method, calcined at different temperatures shows orthorhombic spinel like phase space group-Bb21 m. Castro et al. (1997) synthesized BFO, using the combustion method. Fe_3O_4 , $\text{Ba}(\text{NO}_3)_2$ and BaCO_3 were found as intermediate phases even after the calcination at 700 °C.

The crystallite size of BFO NM, Debye-Scherrer's equation and Williamson and Hall plot (W-h plot) (Fig. 3b) (Vidya et al., 2015b) were employed. Debye-Scherrer's equation is given by

$$D = \frac{0.9\lambda}{\beta \cos\theta} \quad (5)$$

where β ; the diffracted full width at half maximum (FWHM in radian) caused by the crystallites, λ ; the wavelength of X-ray (1.542 Å), θ ; the Bragg angle and k ; is the constant depends on the grain shape (0.90). The high intense diffraction plane (210) is used in Scherrer's equation to calculate the crystallite size and was found to be 16 nm.

The W-h approach considers the case when the domain effect and lattice deformation are both simultaneously operative (Mohanty et al., 2007) and their combined effects give the final line broadening FWHM (β), which is the sum of grain size and lattice distortion. This relation assumes a negligibly small instrumental contribution compared with the sample-dependent broadening. W-h equation may be expressed in the form:

$$\beta \cos\theta = \epsilon(4\sin\theta) + \frac{\lambda}{D} \quad (6)$$

where β ; FWHM in radians is measured for different XRD lines corresponding to different planes, ϵ ; the strain developed and D ; the grain size. The equation represents a straight line between $4\sin\theta$ (X-axis) and $\beta \cos\theta$ (Y-axis) (Fig. 3). The slope of the line gives the strain (ϵ) and intercept (λ/D) of this line on the Y-axis gives grain size (D). The estimated crystallite size was found to be 22 nm. The crystallite size calculated from W-h plot method was slightly higher compared to that of Scherrer's method. The small variation in the crystallite size values from both the methods is mainly because in Scherrer's formula,

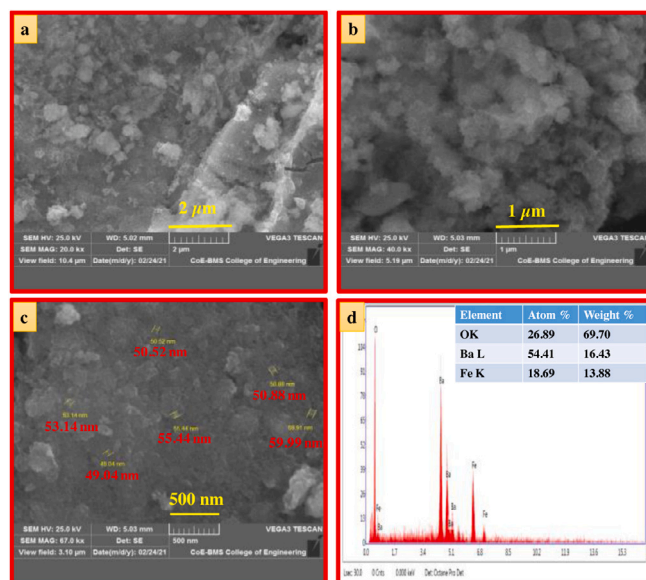


Fig. 4. (a and b) SEM images at different magnification, c) EDAX image of BFO NPs calcined at 500 °C for 3 h.

strain component was assumed to be zero and observed broadening of diffraction peak was considered as a result of reducing grain size. The other structural parameters dislocation density (δ) and stacking fault(Δ) are determined using the following relation (Vidya et al., 2015a).

$$\delta = \frac{1}{D^2} \quad (7)$$

$$\Delta = \left[\frac{2\pi^2}{45(3\sqrt{\tan\theta})} \right] \quad (8)$$

3.2. Morphological analysis of BFO nanoparticles

The surface morphology, formation and distribution of the NPs, elemental composition of the synthesized NMs can be obtained by performing SEM and EDAX analysis. Figs. 4(a), 4(b) and 4(c) shows the SEM images taken at different magnification. The SEM images shows the nonuniform distribution of the crystals with slight agglomeration of the NPs. The average particle size on the surface was found to vary between 49–60 nm. This non uniform shape and size of the NPs may be due to non-uniform distribution of temperature and mass flow in the combustion flame. This type of the non-uniform distribution is a typical characteristic of the combustion synthesized powders. Fig. 4(d) shows the energy dispersive X-ray spectroscopy analysis (EDAX) which confirms the presence of Ba, O and Fe atoms in the host matrix and also the absence of other impurities. The atomic percentage and weight percentage of the elements present in synthesized BFO are provided in the inset table of Fig. 4d.

Transmission electron microscopy (TEM), high resolution TEM (HRTEM) and selected region electron diffraction (SAED) were used to provide further data on the structural details of BFO NPs. Fig. 5(a) shows the TEM image of typical BFO NPs which clearly indicates the presence of irregular shaped agglomerated NPs. HRTEM images also shows the formation of agglomerated NPs (Fig. 5(b)). Fig. 5(c) shows the presence of well ordered lattice of (210) plane with interplanar spacing 0.468 nm. The SAED pattern shows several Debye-Scherrer's rings corresponding to reflections of (210), (610), (612) and (220) of BFO NPs. The rings pattern clearly confirms that the selected BFO NPs are highly crystalline in nature. The estimated crystallite sizes matches well with that of the Scherrer's method.

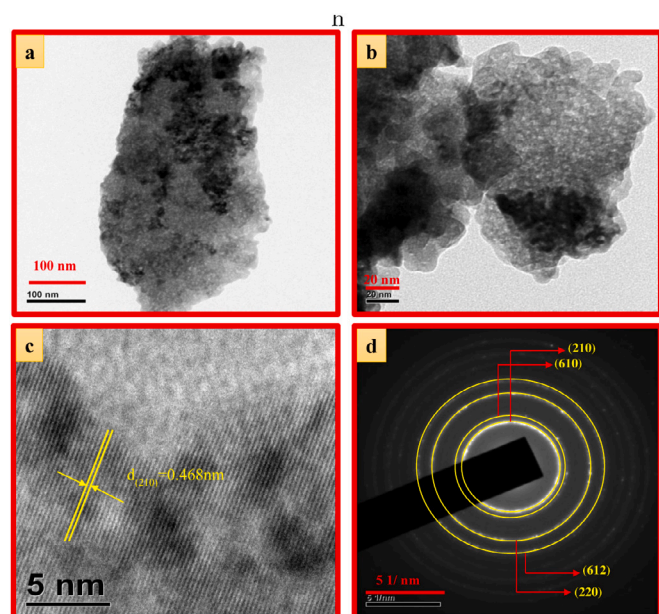


Fig. 5. (a) TEM image,(b) HRTEM image, (c) Lattice fringes and (d) SAED pattern of BFO NPs.

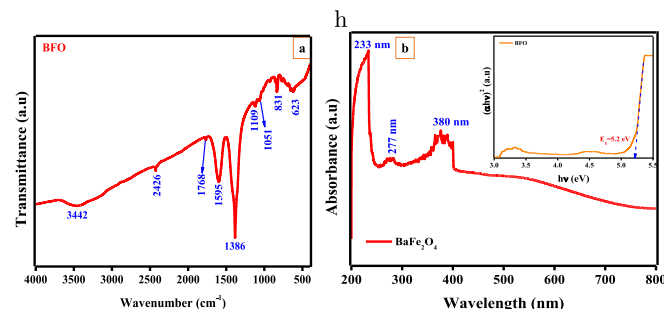


Fig. 6. (a) FTIR spectra and (b) UV-Visible absorption spectra (Inset: Wood and Tauc's plot to find energy band gap of BFO NPs calcined at 500 °C for 3 h.

3.3. FTIR analysis of BFO nanoparticles

FTIR is a technique based on the measurement of the absorption of electromagnetic radiation with wavelengths within the mid-infrared region (4000–400 cm⁻¹). When a molecule absorbs infrared radiation, the dipole moment changes, and the molecule becomes IR active. The location of bands related to the strength and structure of bonds, as well as unique functional groups, can be found in a reported spectrum. Fig. 6(a) shows FTIR spectra recorded in the range 400–4000 cm⁻¹ for BFO NPs calcined at 500 °C for 3 h. These NPs exhibit peaks at 623, 831, 1051, 1109, 1386, 1595, 1768, 2426 and 3442 cm⁻¹. The peak observed at 623 cm⁻¹ is due to the stretching vibration of tetrahedral group complex Fe-O. The peaks at 1051 and 1109 cm⁻¹ are associated with vibrations of M-O-M (M = Ba²⁺ or Fe³⁺) corresponding to the orthorhombic crystalline structure of the prepared BFO NPs. The bands located at 1595 and 3442 cm⁻¹ were assigned to -OH bending and stretching modes respectively corresponding to surface water molecules (Zhang et al., 2012). The band observed at 831 and 2426 cm⁻¹ corresponds to the absorbance of CO₂ from ambient air (Drmosh et al., 2010).

3.4. UV-Visible spectroscopic analysis and direct energy band gap calculation of BFO nanoparticles

UV-Visible spectroscopic method is another relatively facile and low-cost characterization method that is often used for the study of nanoscale materials. It measures the intensity of light reflected/absorbed from a sample and compares it to the intensity of light reflected/absorbed from a reference material. The optical properties of the NMs are sensitive to size, shape, concentration, agglomeration state and refractive index near the nanoparticle surface, which makes UV-Vis spectroscopy an important tool to identify, characterize and investigate these materials. The UV-Visible absorption spectra of BFO NPs in the wavelength range 200–800 nm was shown in Fig. 6(b). The spectra shows prominent absorption band with maximum at 233 and 277 and 380 nm. In the octahedral crystal region, the Fe^{3+} ion had a $3d^5$ configuration with a sextet state. Meanwhile, these transitions were spin symmetry and parity forbidden. Hence very weak crystal field transitions were predicted. Furthermore, the charge transfer transition from O^{2-} to Fe^{3+} is usually associated with a heavy absorption at 275 nm (Xie et al., 2013). In the present study, the strong absorption band observed at 233 nm arises may be due to transition of an electron between valence band to conduction band in the host lattice whereas the less intense absorption band observed at 277 nm corresponds to the charge transfer transition from O^{2-} to Fe^{3+} and 380 nm was expected to arise from transitions involving extrinsic states such as surface states/defects/ impurities (Das et al., 2013; Cao et al., 2004). Generally, NMs synthesized with combustion method possess high surface to volume ratio.

For estimation of band gap in the NMs, the absorbance spectra of BFO in transmission mode were recorded by distributing the particles uniformly in liquid paraffin, in the wavelength range of 200–800 nm. For a direct band gap, the absorption coefficient near the band edge was given by Wood and Tauc's relation (Ley, 1984).

$$\alpha = \frac{A}{hv} (hv - E_g)^{\frac{1}{2}} \quad (9)$$

where α ; absorption co-efficient, $h\nu$; the photon energy, E_g ; the energy gap and A ; the constant depending on the type of transition. From the Eq. (9) $\alpha h\nu = 0$, $E_g = h\nu$. The energy gap is determined by plotting $(\alpha h\nu)^2$ versus $h\nu$ and finding the intercept on the $h\nu$ axis by extrapolating the plot to $(\alpha h\nu)^2 = 0$. Inset of Fig. 6(b) shows the Wood and Tauc plot from which the direct band gap is obtained and was found to be 5.2 eV.

The band gap can also be calculated by using the relation:

$$E_g = \frac{hc}{\lambda} \quad (10)$$

where h is the Plank's constant (6.626×10^{-34} Js), c is the velocity of light (3×10^8 ms $^{-1}$) and λ is wavelength corresponding to maximum intensity in the absorption spectra. The calculated energy band gap was found to be 5.33 eV (Kanagaraj et al., 2016).

3.5. Photoluminescence studies (PL) of BFO nanoparticles (NPs)

Fig. 7(a) depicts room temperature PL emission spectra of BFO NPs corresponding to the wavelength range 460–600 nm excited under 380 nm wavelength. The distinguished spectral peaks are observed at 483 nm, 526 and 569 nm. PL spectra mainly depends on the crystallite size, defects and impurities present in the lattice. The PL properties of ferrites have been widely investigated by many researchers (Teh et al., 2011; Mishra and Qi, 2010; Talukdar et al., 2017; Aisida et al., 2020). However, as per the literature, the PL properties on BFO samples are limited. The chosen PL excitation energy is less than that of the energy band gap. This finding implies that PL for down conversion is not caused by a direct band transition between the valence and conduction bands but originated due to radiative recombination between defective levels (Sangeetha et al., 2019). These acts as defects in the structure

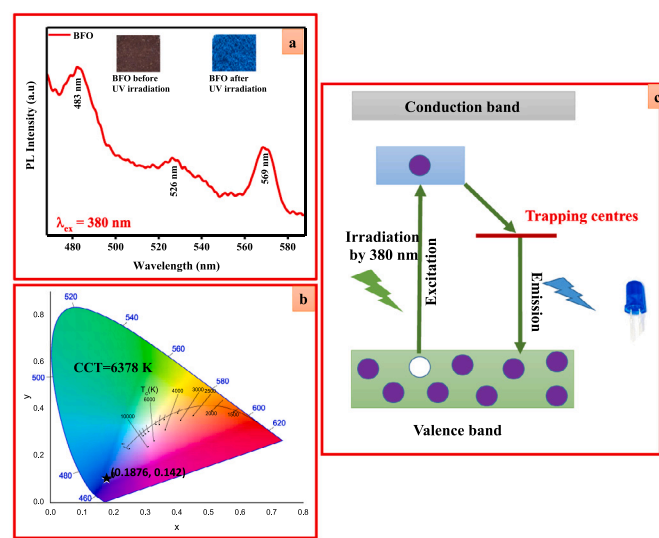


Fig. 7. (a) PL emission spectra excited under 380 nm, (b) CIE and CCT diagram and (c) mechanism of photoluminescence in BFO NPs.

and create electron hole traps within the band gap of BFO, which is responsible for the down conversion and the PL emission peaks as observed. The emission peaks appeared at 526 nm are assigned to $3d^5 \rightarrow 3d^4 4s$ transitions of Fe^{3+} ions in which an electron is excited to the conduction band mainly composed of the 4s orbital of Fe^{3+} from the localized 3d_5 state of Fe^{3+} (Tanaka et al., 2003). The peak at 483 nm gives rise to radiative defects related to interface traps existing at the grain boundaries. The peak at 569 nm is due to singly ionized oxygen vacancy or surface defect because of trap state or deep level emission (Shetty et al., 2017).

The presence of defects and impurities in the system could be the major reason for the luminescence properties of oxide based NMs (Gurushantha et al., 2017). The emission band arises due to the oxygen vacancies defects in BFO NMs. The radiative recombination of a photo generated hole with an electron occupying the oxygen vacancy results in the emission band. When the excitation energy exceeds the band gap of BFO NMs, electron-hole pairs are generated. The electrons were trapped rapidly by the oxygen vacancies thereby producing the F-centres. The holes recombine with the F centres forming the excited states of the emitter. These excited emitters undergo radiative transitions to the ground state. The possible mechanism involved in the emission of the BFO NMs has been demonstrated with the help of the schematic diagram as shown in Fig. 7(c).

One of the most important factors in determining the efficiency of synthesized nanophosphors is Chromaticity coordinates. The emission colour of BFO NMs were investigated by using 1931 CIE (Commission Internationale de L'Eclairage) system. The CIE coordinates (0.1876, 0.142) located in the blue region (Fig. 7b). To identify the technical applicability, correlated colour temperature (CCT) is determined from the CIE coordinates. The CCT describes the colour appearance of light emitted by a light source by comparing it to the colour of light emitted by a reference source when heated to a certain temperature. Lamps with a CCT rating of less than 3200 K are typically referred to as "hot", while those with a CCT of more than 4000 K are typically referred to as "cold". In the present study, the calculated CCT value of BFO NM was found to be 6378 K. This clearly indicates that the present BFO NM can be used as a blue phosphor material which might be a potential candidate for display/cool LED application.

Table 1

Comparison of measured X-ray/gamma shielding properties with that of theory.

SOURCE	^{137}Cs	^{60}Co	^{22}Na	^{56}Ba				
ENERGY (MeV)	0.6615	1.173	1.332	0.511				
μ/ρ (cm^2g^{-1})	Th Ex	0.08 0.08 ± 0.004	0.06 0.55 ± 0.03	0.05 0.05 ± 0.003				
HVL (cm)	Th Ex	1.95 1.96 ± 0.1	2.7 0.27 ± 0.01	2.9 2.92 ± 0.15				
λ (cm)	Th Ex	2.8 2.83 ± 0.14	3.9 0.39 ± 0.02	4.18 4.21 ± 0.21				
Z_{eff}	Th Ex	21.99 21.8 ± 1.09	20.78 20.73 ± 1.04	20.7 20.65 ± 1.03				
$N_e \times 10^{23}$ (electrons g^{-1})	Th Ex	3.07 3.04 ± 0.15	2.90 2.89 ± 0.15	2.89 2.88 ± 0.14				
EABF (mfp = 10 mm)	Th Ex	2.3 1.7 ± 0.09	2.07 1.6 ± 0.08	2.04 1.59 ± 0.08				
KERMA (MeV) $\times 10^{-12}$	Th Ex	1.65 1.65 ± 0.083	2.12 2.13 ± 0.11	2.25 2.25 ± 0.11				
SGR($R\text{m}^2 \text{Ci}^{-1} \text{h}$)	Th Ex	32.29 32.3 ± 1.62	41.72 41.8 ± 2.09	44.37 44.4 ± 2.22				
SAF (g^{-1}) (mfp = 10 mm)	Th (x = 1 mm) Ex (x = 1 mm) Th (x = 5 mm) Ex (x = 5 mm)	1.36 1.33 ± 0.07 0.05 0.04 ± 0.002	0.9 0.9 ± 0.05 0.03 0.03 ± 0.002	0.82 0.82 ± 0.04 0.03 0.02 ± 0.001				
RPE	Th (t = 1) Ex (t = 1) Th (t = 5) Ex (t = 5) Th (t = 10) Ex (t = 10)	30.52 30 ± 1.5 83.35 83 ± 4.15 97.03 97 ± 4.85	22.75 22.5 ± 1.13 72.3 72 ± 3.6 92.23 92.1 ± 4.61	21.43 21.2 ± 1.06 69.89 69.6 ± 3.48 90.81 90.7 ± 4.54	34.27 34.2 ± 1.71 87.66 87.6 ± 4.38 98.44 98.5 ± 4.93	99.55 100 ± 5 99.97 100 ± 5 99.996 100 ± 5	63 53.7 ± 2.69 95.09 97.2 ± 4.86 99.6 99.5 ± 5	47.75 43.6 ± 2.18 92.95 93.9 ± 4.7 99.44 99.6 ± 4.98

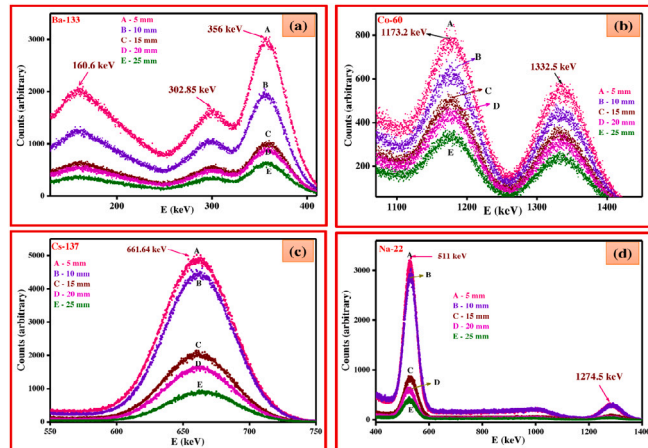


Fig. 8. Measured Gamma ray spectra in BFO NPs using different sources such as Ba-133, Co-60, Cs-137 and Na-22 at various thickness.

3.6. Analysis of measured X-ray/gamma ray shielding properties of BFO nanoparticles

Fig. 8 (a-d) shows the graphical representation of measured gamma ray spectra using different sources such as ^{137}Cs (trace, 0.6615 MeV, 66.6 kBq), ^{60}Co (trace, 1.173 and 1.332 MeV, 111 kBq), ^{22}Na (trace, 0.511, 0.081 MeV, 129 kBq) and ^{133}Ba (synthetic, 0.276 and 0.356 MeV, 146 kBq) for different thickness 5, 10, 15, 20 & 25 mm of BFO NPs. Gamma rays interact with BFO NMs through different interactions such as photoelectric absorption, Compton effect and pair production. In the lower energy region up to 100 keV photoelectric absorption is dominant. Between 100 keV to 2 MeV Compton scattering overtakes the photoelectric absorption and above 2 MeV pair production dominates.

The nature of the gamma ray spectrum is different for different sources. For ^{133}Ba gamma ray source, three high intensity peaks are observed at 160.6, 302.85 and 356 keV. For ^{60}Co source, the gamma ray spectrum consists two peaks at 1173.2 and 1332.5 keV, whereas for ^{137}Cs source, single high intense peak is observed at 661.6 keV. Two high intense peaks are observed at 511 and 1274.5 keV for ^{22}Na source. As the thickness of BFO NPs increases from 5, 10, 15, 20 & 25 mm, the nature of the gamma ray spectrum remains unaltered except the variation in intensity. The intensity of the peak increases with decrease in the thickness of the BFO NM. From the experimental data, the mass attenuation coefficient (MAC) values of BFO NPs at different energies are extracted.

Table 1 gives the comparison of measured shielding properties such as μ/ρ , HVL, TVL, λ , μ , Z_{eff} , N_e , EABF, KERMA, SGR, SAF and RPE with that of the theoretical values in the energy range 0.081–1.332 MeV. Experimental values are presented along with the errors which arises due to counting statistics. It is clearly observed from Table 1 that above 356 keV X-ray/gamma ray interaction energy, the measured shielding parameters agrees well with the theoretical value whereas slight deviation is observed below 356 keV.

Theoretical values are based on the Hubbell data (Hubbell and Seltzer, 1995; Berger, 2010; Gerward et al., 2001) which was used to explain interaction of X-ray/gamma with atoms of size (10^{-6}m). In the present experiment, we have taken the target with atomic size (10^{-9}m). The measured shielding parameters agrees well with the theory above 356 keV X-ray/ gamma-ray interaction. The deviation between the experiment and theory below 356 keV is may be due to atomic size of the target or there may be poor efficiency of NaI detector in the low energy region. It is also expected that the atom /particle size affect the interaction of X-ray/gamma ray with the target medium. Furthermore, an accurate theory is necessary to explain the X-ray/gamma ray interaction with the nanomaterials.

4. Conclusions

We have synthesized BFO NPs of orthorhombic spinel crystal structure of atomic size 16 and 22 nm with energy gap 5.2 eV. Photoluminescence (PL) studies of BFO NPs shows PL emission peaks centred at 483 nm (blue region) which might finds an application in display devices. X-ray/gamma ray shielding properties of BFO NPs were also studied 0.081 to 1.332 MeV. The established shielding properties data for BFO NPs are useful in the field of radiation protection. To use the BFO NPs for the shielding purpose, further detail mechanical properties has to be studied.

Declaration of competing interest

The authors declare that they have no known competing financial interests or personal relationships that could have appeared to influence the work reported in this paper.

Acknowledgement

One of the authors Dr. Sankarshan B. M. would like to thank NIE-CRD for the financial support and encouragement.

References

- Aisida, S.O., Ahmad, I., Zhao, T.-k., Maaza, M., Ezema, F.I., 2020. Calcination effect on the photoluminescence, optical, structural, and magnetic properties of polyvinyl alcohol doped ZnFe₂O₄ nanoparticles. *J. Macromol. Sci. B* 59 (5), 295–308.
- Akther Hossain, A., Seki, M., Kawai, T., Tabata, H., 2004. Colossal magnetoresistance in spinel type Zn 1-x Ni x Fe 2 o 4. *J. Appl. Phys.* 96 (2), 1273–1275.
- Angadi, V.J., Anupama, A., Kumar, R., Somashekharappa, H., Mattepanavar, S., Rudraswamy, B., Sahoo, B., 2017. Dose dependent modifications in structural and magnetic properties of γ -irradiated nanocrystalline Mn_{0.5}Zn_{0.5}Fe₂O₄ ceramics. *Ceram. Int.* 43 (1), 523–526.
- Barros, C.H., Casey, E., 2020. A review of nanomaterials and technologies for enhancing the antibiofilm activity of natural products and phytochemicals. *ACS Appl. Nano Mater.* 3 (9), 8537–8556.
- Bateer, B., Tian, C., Qu, Y., Du, S., Yang, Y., Ren, Z., Pan, K., Fu, H., 2014. Synthesis, size and magnetic properties of controllable MnFe₂O₄ nanoparticles with versatile surface functionalities. *Dalton Trans.* 43 (26), 9885–9891.
- Berger, M., 2010. XCOM: photon cross sections database.
- Bhavikatti, A., Kulkarni, S., Lagashetty, A., 2010. Characterization and electromagnetic studies of nano-sized barium ferrite. *Int. J. Engg. Sci. Tech* 2 (11), 6532–6539.
- Candeia, R., Souza, M., Bernardi, M., Maestrelli, S., Santos, I., Souza, A., Longo, E., 2007. Monoferrite BaFe₂O₄ applied as ceramic pigment. *Ceram. Int.* 33 (4), 521–525.
- Cao, H., Qiu, X., Luo, B., Liang, Y., Zhang, Y., Tan, R., Zhao, M., Zhu, Q., 2004. Synthesis and room-temperature ultraviolet photoluminescence properties of zirconia nanowires. *Adv. Funct. Mater.* 14 (3), 243–246.
- Castro, S., Gayoso, M., Rodriguez, C., 1997. A study of the combustion method to prepare fine ferrite particles. *J. Solid State Chem.* 134 (2), 227–231.
- Chang, S., Kangning, S., Pengfei, C., 2012. Microwave absorption properties of Ce-substituted M-type barium ferrite. *J. Magn. Magn. Mater.* 324 (5), 802–805.
- Chen, D., yan Liu, H., Li, L., 2012. One-step synthesis of manganese ferrite nanoparticles by ultrasonic wave-assisted ball milling technology. *Mater. Chem. Phys.* 134 (2–3), 921–924.
- Chen, H., Zhang, L., Hu, Y., Zhou, C., Lan, W., Fu, H., She, Y., 2020. Nanomaterials as optical sensors for application in rapid detection of food contaminants, quality and authenticity. *Sensors Actuators B* 129135.
- Choi, S.-H., 2017. Unique properties of graphene quantum dots and their applications in photonic/electronic devices. *J. Phys. D: Appl. Phys.* 50 (10), 103002.
- Das, S., Yang, C.-Y., Lu, C.-H., 2013. Structural and optical properties of tunable warm-white light-emitting ZrO₂: Dy³⁺–Eu³⁺ nanocrystals. *J. Am. Ceram. Soc.* 96 (5), 1602–1609.
- Dimri, M.C., Khanduri, H., Agarwal, P., Pahapill, J., Stern, R., 2019. Structural, magnetic, microwave permittivity and permeability studies of barium monoferrite (BaFe₂O₄). *J. Magn. Magn. Mater.* 486, 165278.
- Drmosh, Q., Gondal, M., Yamani, Z., Saleh, T., 2010. Spectroscopic characterization approach to study surfactants effect on ZnO₂ nanoparticles synthesis by laser ablation process. *Appl. Surf. Sci.* 256 (14), 4661–4666.
- El-Khayatt, A., 2017. Semi-empirical determination of gamma-ray kerma coefficients for materials of shielding and dosimetry from mass attenuation coefficients. *Prog. Nucl. Energy* 98, 277–284.
- Gabal, M., Kosa, S., Al Mutairi, T., 2014. Structural and magnetic properties of Ni_{1-x}ZnxFe₂O₄ nano-crystalline ferrites prepared via novel chitosan method. *J. Mol. Struct.* 1063, 269–273.
- Gairola, P., Gairola, S., Kumar, V., Singh, K., Dhawan, S., 2016. Barium ferrite and graphite integrated with polyaniline as effective shield against electromagnetic interference. *Synth. Met.* 221, 326–331.
- Gairola, S., Verma, V., Singh, A., Purohit, L., Kotnala, R., 2010. Modified composition of barium ferrite to act as a microwave absorber in X-band frequencies. *Solid State Commun.* 150 (3–4), 147–151.
- Gatoo, M.A., Naseem, S., Arfat, M.Y., Mahmood Dar, A., Qasim, K., Zubair, S., 2014. Physicochemical properties of nanomaterials: implication in associated toxic manifestations. *BioMed. Res. Int.* 2014.
- Gerward, L., Guibert, N., Jensen, K., Leving, H., 2004. WinXCom- a program for calculating x-ray attenuation coefficients. *Radiat. Phys. Chem. (ISSN: 0969-806X)* 71, 653–654.
- Gerward, L., Guibert, N., Jensen, K.B., Levring, H., 2001. X-ray absorption in matter. *Reengineering XCOM. Radiat. Phys. Chem.* 60 (1–2), 23–24.
- Goswami, P.P., Choudhury, H.A., Chakma, S., Moholkar, V.S., 2013. Sonochemical synthesis and characterization of manganese ferrite nanoparticles. *Ind. Eng. Chem. Res.* 52 (50), 17848–17855.
- Gurushantha, K., Anantharaju, K., Renuka, L., Sharma, S., Nagaswarupa, H., Prashantha, S., Vidya, Y., Nagabhushana, H., 2017. New green synthesized reduced grapheme oxide-ZrO₂ composite as high performance photocatalyst under sunlight. *RSC Adv.* 7 (21), 12690–12703.
- Hamada, I., 2004. X-ray diffraction and IR absorption in the system Co_{0.6}Zn_{0.4}Mn_xFe_{2-x}O₄ before and after γ -irradiation. *J. Magn. Magn. Mater.* 271 (2–3), 318–325.
- Hodala, J.L., Moon, D.J., Reddy, K.R., Reddy, C.V., Kumar, T.N., Ahamed, M.I., Raghu, A.V., 2021. Catalyst design for maximizing C₅₊ yields during fischer-tropsch synthesis. *Int. J. Hydrogen Energy* 46 (4), 3289–3301.
- Hou, X., Feng, J., Xu, X., Zhang, M., 2010. Synthesis and characterizations of spinel MnFe₂O₄ nanorod by seed-hydrothermal route. *J. Alloys Compd.* 491 (1–2), 258–263.
- Hubbell, J.H., Seltzer, S.M., 1995. Tables of X-ray mass attenuation coefficients and mass energy-absorption coefficients 1 keV to 20 MeV for elements Z=1 to 92 and 48 additional substances of dosimetric interest. *Tech. Rep., National Inst. of Standards and Technology-PL*, Gaithersburg, MD (United States).
- Ioan, M.-R., Fugari, V., Bercea, S., Celarel, A., Tugulan, L., Cimpeanu, C., 2018. Co-60 specific Gamma-ray constant determinations for various biological materials involved in radiotherapy procedures, by using GEANT4 and NIST XCOM. *Romanian J. Phys.* 63, 701.
- Jonnalagadda, M., Prasad, V.B., Raghu, A.V., 2021. Synthesis of composite nanopowder through Mn doped ZnS-cds systems and its structural, optical properties. *J. Mol. Struct.* 1230, 129875.
- Kanagaraj, M., Kokila, I.P., Subbulakshmi, N., Kumar, P.S., Rajesh, A.L., Arumugam, S., 2016. A systematic investigation of structural, optical and magnetic properties of pristine BaFe₂O₄, Mg and Mg, Cs co-doped in BaFe_{2-x}Mg_xO₄ and Ba_{1-x}Cs_xFe_{2-y}Mg_yO₄ spinel nanoferrites. *Indian J. Pure Appl. Phys.* 54.
- Kannan, K., Radhika, D., Reddy, K.R., Raghu, A.V., Sadasisvuni, K.K., Palani, G., Gurushankar, K., 2021. Gd³⁺ and Y³⁺ co-doped mixed metal oxide nanohybrids for photocatalytic and antibacterial applications. *Nano Express* 2 (1), 010014.
- Kaphle, A., Navya, P., Umapathi, A., Daima, H.K., 2018. Nanomaterials for agriculture, food and environment: applications, toxicity and regulation. *Environ. Chem. Lett.* 16 (1), 43–58.
- Karim, A., Shirsath, S.E., Shukla, S., Jadhav, K., 2010. Gamma irradiation induced damage creation on the cation distribution, structural and magnetic properties in Ni-Zn ferrite. *Nucl. Instrum. Methods Phys. Res. B* 268 (17–18), 2706–2711.
- Karthik, K., Reddy, C.V., Reddy, K.R., Ravishankar, R., Sanjeev, G., Kulkarni, R.V., Shetti, N.P., Raghu, A., 2019. Barium titanate nanostructures for photocatalytic hydrogen generation and photodegradation of chemical pollutants. *J. Mater. Sci., Mater. Electron.* 30 (23), 20646–20653.
- Kumar, P., 2019. Ultrathin 2D nanomaterials for electromagnetic interference shielding. *Adv. Mater. Interfaces* 6 (24), 1901454.
- Kumar, R.J., Naresh, U., Ramaprasad, T., Prakash, M., 2018. Structural morphological properties of BaFe₂O₄ nano-particles. *J. Emerg. Technol. Innov. Res.* 5 (7), 34–38.
- Ley, L., 1984. Photoemission and optical properties. *Phys. Hydrog. Amorph. Silicon II* 61–168.
- Li, Q., Pang, J., Wang, B., Tao, D., Xu, X., Sun, L., Zhai, J., 2013. Preparation, characterization and microwave absorption properties of barium-ferrite-coated fly-ash cenospheres. *Adv. Powder Technol.* 24 (1), 288–294.
- Liu, J.-H., Zhang, G.-H., Wang, Z., 2018. Co₂ absorption of powdered Ba₂Fe₂O₅ with different particle size. *High Temp. Mater. Process.* 37 (9–10), 1001–1006.
- Mande, V.K., Kounsalye, J.S., Vyawahare, S., Jadhav, K., 2019. Effect of γ -radiation on structural, morphological, magnetic and dielectric properties of Zn–Cr substituted nickel ferrite nanoparticles. *J. Mater. Sci., Mater. Electron.* 30 (1), 56–68.
- Mane, M.L., Sundar, R., Ranganathan, K., Oak, S., Jadhav, K., 2011. Effects of Nd³⁺ YAG laser irradiation on structural and magnetic properties of Li_{0.5}Fe₂O₄. *Nucl. Instrum. Methods Phys. Res. B* 269 (4), 466–471.
- Manjunatha, H.C., 2014. A study of photon interaction parameters in lung tissue substitutes. *J. Med. Phys./Assoc. Med. Phys. India* 39 (2), 112.

- Manjunatha, H.C., 2015. Influence of gamma irradiation on conductivity of YBa₂Cu₃O₇. *Radiat. Phys. Chem.* 113, 24–27.
- Manjunatha, H.C., 2017. A study of gamma attenuation parameters in poly methyl methacrylate and kapton. *Radiat. Phys. Chem.* 137, 254–259.
- Manjunatha, H.C., Chandrika, B., Seenappa, L., Hanumantharayappa, C., 2016. Study of gamma attenuation properties of tungsten copper alloys. *Int. J. Nucl. Energy Sci. Technol.* 10 (4), 356–368.
- Manjunatha, H.C., Rudraswamy, B., 2011. Computation of CT-number and Z_(eff) in teeth. *Health Phys.* 100, 592–599.
- Manjunatha, H.C., Rudraswamy, B., 2012. Energy absorption and exposure build-up factors in hydroxyapatite. *Radiat. Meas.* 47 (5), 364–370.
- Manjunatha, H.C., Rudraswamy, B., 2013. Study of effective atomic number and electron density for tissues from human organs in the energy range of 1 keV–100 GeV. *Health Phys.* 104 (2), 158–162.
- Manjunatha, H., Sathish, K., Seenappa, L., Gupta, D., Raj, S.A.C., 2019. A study of X-ray, gamma and neutron shielding parameters in si-alloys. *Radiat. Phys. Chem.* 165, 108414.
- Manjunatha, H.C., Seenappa, L., Chandrika, B., Hanumantharayappa, C., 2017. A study of photon interaction parameters in barium compounds. *Ann. Nucl. Energy* 109, 310–317.
- Mishra, D.K., Qi, X., 2010. Energy levels and photoluminescence properties of nickel-doped bismuth ferrite. *J. Alloys Compd.* 504 (1), 27–31.
- Mohanty, P., Kim, B., Park, J., 2007. Synthesis of single crystalline europium-doped ZnO nanowires. *Mater. Sci. Eng. B* 138 (3), 224–227.
- Naseri, M.G., Saion, E.B., Ahangar, H.A., Hashim, M., Shaari, A.H., 2011. Synthesis and characterization of manganese ferrite nanoparticles by thermal treatment method. *J. Magn. Magn. Mater.* 323 (13), 1745–1749.
- Ohlan, A., Singh, K., Chandra, A., Dhawan, S., 2008. Conducting ferromagnetic copolymer of aniline and 3, 4-ethylenedioxothiophene containing nanocrystalline barium ferrite particles. *J. Appl. Polym. Sci.* 108 (4), 2218–2225.
- Patra, J.K., Baek, K.-H., 2014. Green nanobiotechnology: factors affecting synthesis and characterization techniques. *J. Nanomater.* 2014.
- Pellico, J., Gawne, P.J., de Rosales, R.T., 2021. Radiolabelling of nanomaterials for medical imaging and therapy. *Chem. Soc. Rev.*
- Peymanfar, R., Rahmaniaghieh, M., Ghaffari, A., Yassi, Y., 2018. Preparation and identification of BaFe₂O₄ nanoparticles by the sol-gel route and investigation of its microwave absorption characteristics at ku-band frequency using silicone rubber medium. In: Multidisciplinary Digital Publishing Institute Proceedings, vol. 2. (17), p. 5234.
- Qiu, J., Gu, M., Shen, H., 2005. Microwave absorption properties of Al-and Cr-substituted M-type barium hexaferrite. *J. Magn. Magn. Mater.* 295 (3), 263–268.
- Rafique, M.Y., Ellahi, M., Iqbal, M.Z., Pan, L., et al., 2016. Gram scale synthesis of single crystalline nano-octahedron of NiFe₂O₄: Magnetic and optical properties. *Mater. Lett.* 162, 269–272.
- Rammah, Y.S., Ali, A.A., El-Mallawany, R., El-Agawany, F.I., 2020. Fabrication, physical, optical characteristics and gamma-ray competence of novel bismo-borate glasses doped with yb_2o_3 rare earth. *Phys. B Condens. Matter* 583, 412055.
- Raut, S.D., Awasarmol, V., Gaikwad, D., Pawar, P., 2017. Effective atomic number and effective electron density for barium ferrite and barium hexaferrite in the energy range 122–1330 kev. *Nucl. Chem. Nucl. Probes* 102–103.
- Reddy, K.R., Jyothi, M., Raghu, A., Sadhu, V., Naveen, S., Aminabhavi, T.M., 2020. Nanocarbons-supported and polymers-supported titanium dioxide nanostructures as efficient photocatalysts for remediation of contaminated wastewater and hydrogen production. In: Nanophotocatalysis and Environmental Applications. Springer, pp. 139–169.
- Reddy, B.C., Manjunatha, H., Vidya, Y., Sridhar, K., Pasha, U.M., Seenappa, L., Mahendrakumar, C., Sadashivamurthy, B., Dhananjaya, N., Sankarshan, B., et al., 2021. Synthesis and characterization of multi functional nickel ferrite nano-particles for X-ray/gamma radiation shielding, display and antimicrobial applications. *J. Phys. Chem. Solids* 159, 110260.
- Rudraswamy, B., Dhananjaya, N., Manjunatha, H.C., 2010. Measurement of absorbed dose rate of gamma radiation for lead compounds. *Nucl. Instrum. Methods Phys. Res. A* 619 (1–3), 171–173.
- Sangeetha, A., Nagabhushana, B., et al., 2019. Comparative study of photoluminescence of single and mixed phase ZrTiO₄ prepared by solution combustion and polymeric precursor method. *J. Mol. Struct.* 1179, 126–131.
- Sayed, M., Lakshminarayana, G., Kityk, I., Mahdi, M., 2017. Evaluation of shielding parameters for heavy metal fluoride based tellurite-rich glasses for gamma ray shielding applications. *Radiat. Phys. Chem.* 139, 33–39.
- Seenappa, L., Manjunatha, H.C., Chandrika, B., Hanumantharayappa, C., 2017. A study of shielding properties of X-ray and gamma in barium compounds. *J. Radiat. Prot. Res.* 42 (1), 26–32.
- Shanmugan, S., Gorjani, S., Elsheikh, A.H., Essa, F.A., Omara, Z.M., Raghu, A.V., 2020. Investigation into the effects of SiO₂/TiO₂ nanolayer on the thermal performance of solar box type cooker. *Energy Sour. A Recovery Util. Environ. Effects* 1–14.
- Shetty, K., Lokesh, S., Rangappa, D., Nagaswarupa, H., Nagabhushana, H., Anantharaju, K., Prashantha, S., Vidya, Y., Sharma, S., 2017. Designing MgFe₂O₄ decorated on green mediated reduced graphene oxide sheets showing photocatalytic performance and luminescence property. *Physica B* 507, 67–75.
- Singh, K., Ohlan, A., Saini, P., Dhawan, S., 2008. Poly (3, 4-ethylenedioxothiophene) γ -Fe₂O₃ polymer composite-super paramagnetic behavior and variable range hopping 1d conduction mechanism-synthesis and characterization. *Polym. Adv. Technol.* 19 (3), 229–236.
- Slusarek, B., Zakrzewski, K., 2012. Magnetic properties of permanent magnets for magnetic sensors working in wide range of temperature. *Przegl. Elektrotech. (Electr. Rev.)* 88, 123.
- Srinivas, M., Venkata, R.C., Kakarla, R.R., Shetti, N.P., Reddy, M., Anjanapura, V.R., 2019. Novel Co and Ni metal nanostructures as efficient photocatalysts for photodegradation of organic dyes. *Mater. Res. Express* 6 (12), 125502.
- Suárez-Iglesias, O., Collado, S., Oulego, P., Díaz, M., 2017. Graphene-family nanomaterials in wastewater treatment plants. *Chem. Eng. J.* 313, 121–135.
- Suresh, K.C., Manjunatha, H.C., Rudraswamy, B., 2007. Study of zeff for DNA, RNA and retina by numerical methods. *Radiat. Prot. Dosim.* (ISSN: 0144-8420) 128 (3), 294–298. <http://dx.doi.org/10.1093/rpd/ncm382>, arXiv:<https://academic.oup.com/rpd/article-pdf/128/3/294/4534800/ncm382.pdf>.
- Suresh, K.C., Manjunatha, H.C., Rudraswamy, B., 2008. Study of Z eff for DNA, RNA and RETINA by numerical methods. *Radiat. Prot. Dosim.* 128 (3), 294–298.
- Talukdar, S., Mandal, D., Mandal, K., 2017. Surface modification of Cobalt ferrite nano-hollowspheres for inherent multiple photoluminescence and enhanced photocatalytic activities. *Chem. Phys. Lett.* 672, 57–62.
- Tanaka, K., Nakashima, S., Fujita, K., Hirao, K., 2003. High magnetization and the faraday effect for ferrimagnetic zinc ferrite thin film. *J. Phys.: Condens. Matter* 15 (30), L469.
- Teh, G.B., Wong, Y.C., Tilley, R.D., 2011. Effect of annealing temperature on the structural, photoluminescence and magnetic properties of sol-gel derived magnetoplumbite-type (M-type) hexagonal strontium ferrite. *J. Magn. Magn. Mater.* 323 (17), 2318–2322.
- Thibeault, S.A., Kang, J.H., Sauti, G., Park, C., Fay, C.C., King, G.C., 2015. Nanomaterials for radiation shielding. *Mrs Bull.* 40 (10), 836–841.
- Valenzuela, R., 2012. Novel applications of ferrites. *Phys. Res. Int.* 2012.
- Vidya, Y., Anantharaju, K., Nagabhushana, H., Sharma, S., 2015a. Euphorbia tirucalli mediated green synthesis of rose like morphology of Gd₂O₃: Eu³⁺ red phosphor: structural, photoluminescence and photocatalytic studies. *J. Alloys Compd.* 619, 760–770.
- Vidya, Y., Anantharaju, K., Nagabhushana, H., Sharma, S., Nagaswarupa, H., Prashantha, S., Shivakumara, C., et al., 2015b. Combustion synthesized tetragonal ZrO₂: Eu³⁺ nanoporphors: structural and photoluminescence studies. *Spectrochimica Acta A Mol. Biomol. Spectroscopy* 135, 241–251.
- Xie, T., Xu, L., Liu, C., Wang, Y., 2013. Magnetic composite ZnFe₂O₄/SrFe12O₁₉: Preparation, characterization, and photocatalytic activity under visible light. *Appl. Surf. Sci.* 273, 684–691.
- Zhang, F., Yuan, C., Lu, X., Zhang, L., Che, Q., Zhang, X., 2012. Facile growth of mesoporous co₃O₄ nanowire arrays on Ni foam for high performance electrochemical capacitors. *J. Power Sources* 203, 250–256.